PAPER

Check for updates

Hydrogen evolution reaction evidenced for Mo$_2$O$_2$S$_2$-thiosemicarbazone coordination complexes†

Jordi Buils, [a,b] Sergiu Calancea, [c] Yasmine Bouaouni, [c] Roa AlChamandi, [c] Maxime Laurans, [c] Diana Cebotari, [c,d] Jérôme Marrot, [c] Mathieu Frégnaux, [c] Aurelian Gulea, [d] Mireia Segado-Centellas, *[b] Carles Bo [a,b] and Sébastien Floquet *[c]

In this study, a family of 7 dinuclear and tetranuclar complexes formed between the thiocation [Mo$_2$O$_2$S$_2$]$^{2+}$ and various bis-thiosemicarbazone ligands are studied towards their properties for the reduction of protons into hydrogen in aqueous medium. The HER properties of the complexes in the form of modified electrodes are evidenced in the 1–4 pH range and the impact of the variation of ligand as well as the nuclearity of the complexes are investigated. DFT studies allowed to elucidate the HER mechanism through a Volmer–Tafel mechanism involving a first step of reduction of the Mo cluster with 2 electrons, a first protonation leading to the formation of a molybdenum hydride, a second protonation on the thiolate of the nearby thiosemicarbazone ligand associated with the decoordination of Mo and then the combination of this proton with a hydride to form H$_2$ and regenerate the initial complex.

Introduction

Hydrogen is considered as one the most suitable energy vector of the future for the large-scale storage of renewable electricity but its formation requires the use of catalysts, often based on noble metals. In the search for cheaper and efficient catalysts, molybdenum sulphides materials[1–7] as well as coordination complexes based on [Mo$_3^{IV}$S$_4$]$^{4+}$ and [Mo$_2^V$O$_2$S$_2$]$^{2+}$ clusters have proved particularly promising for the Hydrogen Evolution Reaction (HER).[8–19] In particular, Miras and coworkers recently evidenced remarkable properties in terms of overpotential, stability and efficiency for the complexes [Mo$_2$O$_2$S$_2$(S$_2$)$_2$]$^{2-}$ and [Mo$_2$O$_2$S$_2$(S$_2$)(S$_4$)]$^{2-}$ deposited on the surface of a carbon electrode.[19]

In previous work, we have demonstrated HER activity for a family of cyclic oxothiomolybdic compounds formed by the self-assembly of [Mo$_2$O$_2$S$_2$]$^{2+}$ clusters around organic carboxylate ligands.[8–12] These compounds have been shown to be active both in solution and deposited on electrodes, in both organic and aqueous media. Through these studies, we have demonstrated in particular that the presence of bridging sulphides between the two Mo(v) atoms is important, probably to stabilise a lower oxidation state of Mo in one step of the mechanism,[11] and the ligand embedded in the rings likely functions as a proton relay, with its activity increasing as the ligand becomes more basic[12] but the mechanism has not been elucidated despite these important clues.

In another topic, we have recently demonstrated the formation of complexes associating the [Mo$_2$O$_2$S$_2$]$^{2+}$ cluster with thiosemicarbazone ligands.[20] These complexes can provide interesting biological properties[21,22] and their nuclearity can vary depending on the nature of the ligands. In 2023, we demonstrated for instance the formation of di-nuclear and tetranuclear complexes with bis-thiosemicabazone ligands depending on the nature of the spacer groups used between the thiosemicarbazone moieties (see Fig. 1).[23]

In addition to their biological relevance, some recent studies have reported proton-to-hydrogen reduction properties in cobalt,[24–26] nickel[25,27–29] and zinc[30] thiosemicarbazone complexes. Given the HER properties observed in various [Mo$_2$O$_2$S$_2$]$^{2+}$ cluster-based compounds, it seemed natural for

^{a}Institute of Chemical Research of Catalonia (ICIQ-CERCA), The Barcelona Institute of Science and Technology, Av. Països Catalans 16, 43007 Tarragona, Spain
^{b}Departament de Química Física i Inorgànica, Universitat Rovira i Virgili (URV), Marcel li Domingo, 43007 Tarragona, Spain. E-mail: mireia.segado@urv.cat
^{c}Institut Lavoisier de Versailles, CNRS UMR 8180, Univ. Versailles Saint Quentin en Yvelines, Université Paris-Saclay, 45 av. des Etats-Unis, 78035 Versailles cedex, France. E-mail: sebastien.floquet@uvsq.fr
^{d}State University of Moldova, 60 Alexei Mateevici str., MD-2009 Chisinau, Republic of Moldova

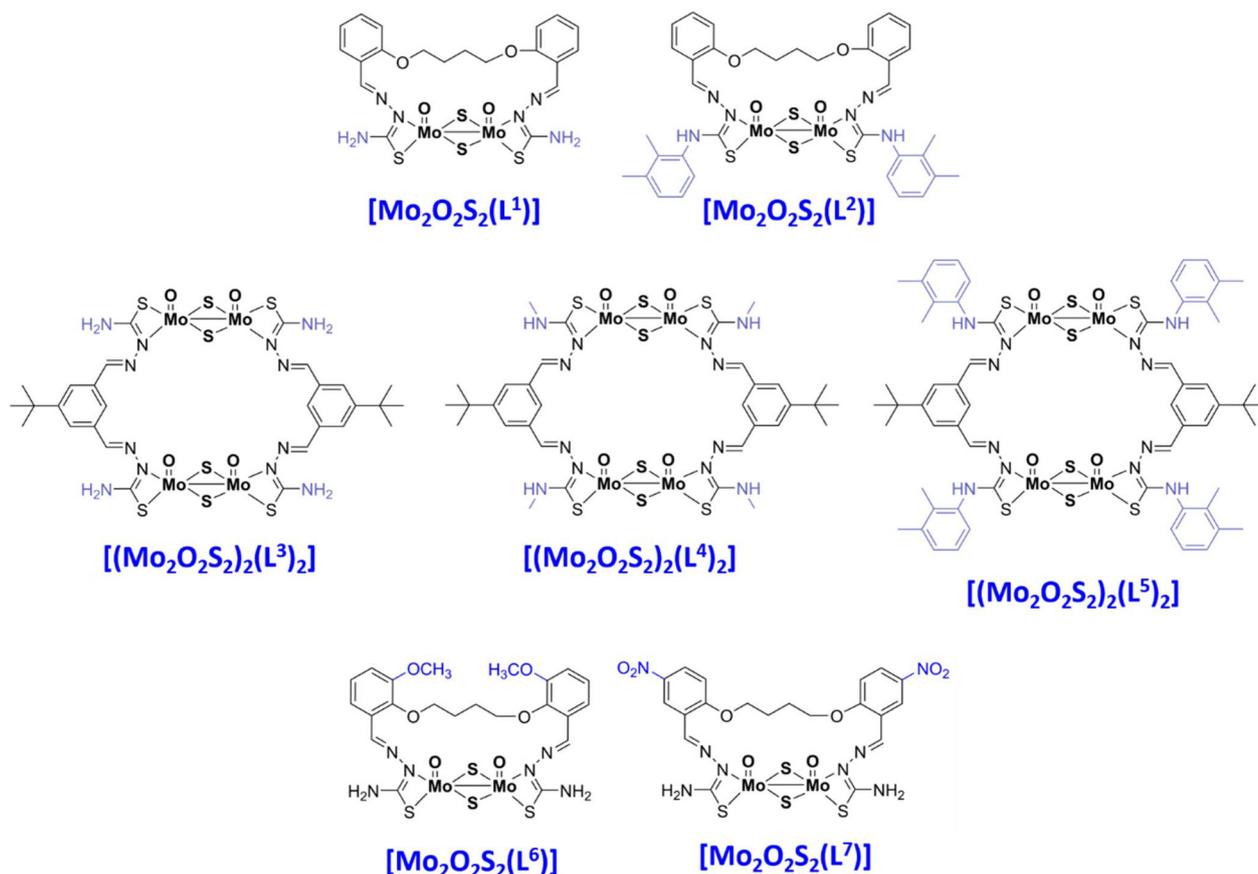**Fig. 1** Schematic drawings of the complexes used in this study.

us to test this property in a series of $[Mo_2O_2S_2]^{2+}$-thiosemicarbazone complexes. This was particularly compelling since these ligands contain coordinating sulfur atoms and multiple potentially protonable nitrogen and sulfur sites—two key factors we had identified in our studies on Mo rings.

As demonstrated by Orio for nickel and cobalt-thiosemicarbazone complexes, the nature of the thiosemicarbazone ligands, especially when substituted by donor or acceptor groups in different positions and the nuclearity of the complexes influence the electrochemical properties and the electrocatalytic properties for protons reduction.[26,28,29] In this study, we focused on 7 complexes drawn in Fig. 1 resulting from the combination of $[Mo_2O_2S_2]^{2+}$ clusters with flexible or rigid bis-thiosemicarbazone ligands. Five of these complexes were already reported in 2023 [23] and this study aimed at evaluating their HER properties, if present, while also exploring the potential influence of the complexes nuclearity and the nature of the ligands. Extending this series, two more complexes were synthesized with modified ligands bearing donor and acceptor groups in order to understand how these changes influence HER activity.

Lastly, a mechanistic investigation using density functional theory (DFT) was carried out to clarify the HER mechanism in the most efficient complex.

Experimental section

Materials and methods

All chemicals were analytical grade and used without any further purification. IR spectra were recorded on a 6700 Fourier Transform Nicolet spectrophotometer, using diamond ATR technique in the range 400–4000 cm^{-1}. The elemental analysis for C, H, N and S were performed by Biocis company at Chatenay-Malabry, France. ^{1}H, NMR spectra were measured at 298 K on Bruker Avance 400 MHz spectrometer with 5 mm BBI probe head at 9.4 T. All samples were solubilised in CD$_3$CN or in DMSO-d$_6$ deuterated solvent. Chemical shifts are reported to tetramethylsilane (TMS) as internal standard.

Single crystal X-ray diffraction

The single-crystal X-ray diffraction data were collected for complex $[\mathbf{Mo_2O_2S_2(L^6)}]$, on a Bruker Apex Duo diffractometer with molybdenum radiation (MoK$_\alpha$, λ = 0.71073 Å) or Kappa X8 APPEX II Bruker diffractometer with graphite-monochromated MoKα radiation (λ = 0.71073 Å). By doing φ and ω scans of narrow (0.5°) frames at 200 K. Crystals were mounted on a CryoLoop (Hampton Research) with Paratone-N (Hampton Research) as cryoprotectant and then flashfrozen in a nitrogen-gas stream at 200 K. The empirical absorption correction

was applied using the SADABS program.[31] The structures were solved by direct methods and refined by full-matrix least-squares treatment against $|F|^2$ in anisotropic approximation with SHELX 2014/7 set[32] using ShelXle program.[33] Hydrogen atoms were located on a difference Fourier map and introduced into the calculations as a riding model with isotropic thermal parameters. Crystallographic data are given in Tables S1 and S2 (ESI†), while the structure has been deposited at the Cambridge Crystallographic Data Centre under the reference CCDC-2417543.†

Electrochemical studies in solution

Cyclic voltammetric (CV) experiments on Mo-complexes (0.5×10^{-3} mol L^{-1}) were recorded in 0.1 mol L^{-1} Bu$_4$NPF$_6$–DMF electrolyte at ν = 0.1 V s^{-1} with an Autolab PGSTAT12 potentiostat/galvanostat associated with a GPES electrochemical analysis system (EcoChemie). Measurements were performed at room temperature in a conventional single compartment cell with an Ag/AgCl reference electrode, platinum gauze of large surface area and a static surface glassy carbon disk working electrode (∅ 3 mm). The solutions were deaerated thoroughly for at least 10 minutes with pure argon and kept under a positive pressure of this gas during the experiments.

Electrochemical studies on modified electrodes

The electrodes were modified by drop casting of an ink containing the Mo-complexes at the surfaces of glassy carbon electrodes. Catalytic inks were prepared by solubilising around 10 mg of the complexes in 1500 µL of dichloromethane, then adding 20 mg of vulcanised carbon and 100 µL of Nafion polymer. The mixture was homogenised by ultrasound for 15 minutes, then two drops were deposited on the electrode surface and air-dried.

The electrocatalytic activity towards reduction of protons (HER) was measured by linear sweep voltammetry (LSV) in aqueous medium. LSV reduction cycles between 0 and −1.2 V relative to the Ag|AgCl electrode (Ag|AgCl|KCl sat.| glass frit), in HCl/NaCl solutions from pH = 7 to pH = 1 at a scan rate of 50 mV s^{-1} were carried out. All measurements were performed under nitrogen atmosphere. In order to facilitate the detachment of the hydrogen bubbles from the electrode surface, a rotating electrode was used (2000 tr mn^{-1}).

Quantitative hydrogen evolution analysis. The release of H$_2$ was monitored using a gas-tight conical cell containing the modified rotating electrode, the Ag|AgCl|KCl sat.| glass frit reference and, as counter-electrode, a bare carbon in an HCl/NaCl solution at pH = 1. The cell was connected to a gas chromatograph to identify and quantify the hydrogen produced during chronopotentiometry carried out at −10 mA cm^{-2} (−0.4 V).

Energy – dispersive X – ray spectroscopy (EDX) and scanning electron microscope (SEM)

SEM images were acquired on a Thermo Fisher Scientific Axia ChemiSEM instrument with a tungsten filament and an energy-dispersive X-ray spectroscopy (EDS) detector at an accelerating voltage of 15 kV and a 10 mm working distance. The

quantification is performed with the standard library provided by the constructor using Kα lines except for Mo (Lα line). Samples were gold-sputtered (12 nm) before analysis.

XPS studies

For the powder analysis, few milligrams Mo complexes were dispersed in 1 mL of dichloromethane and a 20 µL of this solution was drop casted on silicon substrate. The dried droplet obtained was then characterized by XPS. Regarding the catalytic ink, XPS analyses were conducted directly on top of the electrode before and after HER. XPS measurements were performed on a Thermo-Fisher Scientific Nexsa equipped with a monochromated Al-Kα anode (1486.6 eV) and a dual flood gun (low energy electron and ion). High energy resolution spectral windows of interest were recorded with a 400 µm spot size. The photoelectron detection was performed perpendicularly to the surface using a constant analyzer energy (CAE) mode (20 eV pass energy) and a 0.1 eV energy step. The S 2p and Mo 3d core levels spectra presented in this study were reconstructed using the Thermofisher Scientific Avantage© software after a Shirley type (i.e. smart background) background subtraction.

Computational details

The molecular geometry of all the complexes underwent full optimization utilizing a Density Functional Theory (DFT) method in the Amsterdam density functional package (SCM AMS version 2021.101) with the Slater[34] TZP basis set from the AMS library. The optimization process employed the Becke and Perdew exchange–correlation functional (BP86 [35,36]) in conjunction with the dispersion correction D3 from Grimme.[37] Relativistic corrections were considered using the scalar Zero Order Regular Approximation (ZORA).[38] To account for water solvation effects, the continuous Conductor like Screening Model (COSMO)[39] was used, incorporating the Klamt atomic radii.[40] Furthermore, analytical vibrational frequencies were computed for the stationary points to characterize their nature as minima on the energy surface. Transition states and IRC calculations were performed with the methods implemented in the Amsterdam density functional package (SCM AMS version 2021.101). A dataset collection with all the DFT calculations is available in the ioChem-BD repository through the following link https://dx.doi.org/10.19061/iochem-bd-1-371.[41]

Synthetic procedures

The 5 complexes [**Mo$_2$O$_2$S$_2$(L^1)**], [**Mo$_2$O$_2$S$_2$(L^2)**], [**(Mo$_2$O$_2$S$_2$)$_2$(L^3)$_2$**], [**(Mo$_2$O$_2$S$_2$)$_2$(L^4)$_2$**], and [**(Mo$_2$O$_2$S$_2$)$_2$(L^5)$_2$**] were prepared as reported by Cebotari et al.[23] The ligands H$_2$L^6 (R = 3-OMe) and H$_2$L^7 (R = 5-NO$_2$) were synthesized in two steps according to the general Scheme 1 from the corresponding commercial substituted salicylaldehydes.

Synthesis of bis-aldehydes

The 2-[4-(2-formylphenoxy)butoxy]benzaldehyde was synthesized according to the protocol described in the literature.[42]
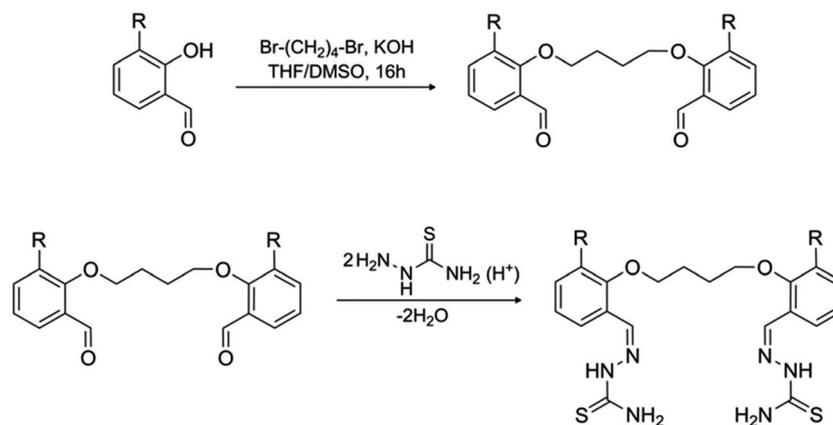
Scheme 1 Synthesis scheme for the two-step preparation of ligands.

2,2′-[Butane-1,4-diylbis(oxy)]bis(3-methoxybenzaldehyde) and 2,2′-[butane-1,4-diylbis(oxy)]bis(5-nitrobenzaldehyde). In a 500 mL flask, were added 0.05 mol of 2-hydroxy-3-methoxybenzaldehyde or 0.03 mol of 2-hydroxy-5-nitrobenzaldehyde, 0.1 mol of K_2CO_3 or 0.06 mol of K_2CO_3 in the case of 2-hydroxy-5-nitrobenzaldehyde and 250 mL of CH_3CN. The mixture was stirred for 30 minutes, then 0.025 mol of 1,4-dibromobutane or 0.015 mol is added dropwise. The yellow mixture was stirred and heated at reflux (60 °C) for 24 hours. After cooling to room temperature, the solvent was evaporated and the aldehyde precipitates by the addition of water. The product was purified by recrystallization from ethanol.

2,2′-[Butane-1,4-diylbis(oxy)]bis(3-methoxybenzaldehyde) (50% yield). ^1H RMN (300 MHz, CD_3CN) δ: 10.35 (s, 2H, 2CH=O), 7.25 (m, 2H, Ar), 7.23 (m, 2H, Ar), 7.07 (t, 2H, Ar), 4.17 (s, 4H, 2CH₂), 3.82 (s, 6H, OCH₃), 2.70 (d, 4H, 2CH₂).

2,2′-[Butane-1,4-diylbis(oxy)]bis(5-nitrobenzaldehyde) (45% yield). ^1H RMN (300 MHz, DMSO-d_6) δ: 10.32 (s, 2H, 2CH=O), 8.47 (m, 2H, Ar), 8.40 (m, 2H, Ar), 7.47 (t, 2H, Ar), 4.41 (s, 4H, 2CH₂), 2.08 (d, 4H, 2CH₂).

Synthesis of the ligands H_2L^6 and H_2L^7

In a 100 mL flask, one equivalent of bis-aldehyde (3.35×10^{-3} mol) and two equivalents thiosemicarbazide (6.7×10^{-3} mol) were dissolved in 50 mL of methanol. Then 2–3 drops of acetic acid were added and the resulting solution was heated under reflux for 24 hours. The reaction mixture was cooled in an ice bath. The resulting yellow precipitates were filtered on, dried by washing with ethanol and diethyl ether and dried under vacuum.

H_2L^6 (yield 82%). ^1H RMN (300 MHz, DMSO d_6, see Fig. 5B) δ: 11.4 (s, 2H, 2NH), 8.16 (s, 2H, NH₂), 7.94 (s, 2H, NH₂), 8.4 (s, 2H, 2CH=N), 7.05 (d, 2H, Ar), 7.70 (t, 2H, Ar), 7.06 (d, 2H, Ar), 3.97 (s, 4H, 2CH₂), 3.79 (s, 6H), 1.99 (s, 4H, 2CH₂).

H_2L^7. Despite our efforts we were not able to isolate the pure ligand H_2L^7. The presence of nitro groups clearly reduces the reactivity of the bis-aldehyde and the protonated functions on the ligand and the thiosemicarbazide renders very difficult the

separation of products by chromatography. For the best of our results we got a mixture between the ligand and the starting bis-aldehyde in 70/30 proportions. The ^1H NMR spectrum is given in ESI (Fig. S1A†).

Synthesis of complexes $[Mo_2O_2S_2(L^6)]$ and $[Mo_2O_2S_2(L^7)]$

To 20 mL of a DMF solution containing 0.833 mmol of ligand H_2L^6 (for H_2L^7, the 70% purity is taken into account and we supposed that the bis aldehyde cannot react, or much less, with Mo precursor) with 20 mL of DMF solution containing 0.166 mmol of $K_{2-x}(NMe_4)_x[I_2Mo_{10}O_{10}S_{10}(OH)_{10}(H_2O)_5]\cdot20H_2O$ (0.833 mmol of cluster $[Mo_2O_2S_2]^{2+}$) was added dropwise. The obtained red-orange solutions were stirred for 4 h, filtered if necessary, and left at room temperature.

X-ray diffraction suitable orange single crystals of $[\mathbf{Mo_2O_2S_2(L^6)}]$ (60% yield) were obtained by slow evaporation of DMF after one week at room temperature. ^1H NMR (300 MHz, DMSO d_6, Fig. 5C) δ: 9.12 (s, 4H, NH₂), 9.58 (s, 2H, 2CH=N), 7.15 (m, 2H, Ar), 7.91 (dd, 2H, Ar), 7.06 (m, 2H, Ar), 4.26 (m, 2H, CH₂), 3.86 (s, 6H, 2CH₃), 4.08 (m, 2H, CH₂), 1.95 (m, 4H, 2CH₂). Elemental analysis calculated for $[\mathbf{Mo_2O_2S_2(L^6)}]\cdot2DMF$: C, 35.90; H, 4.30; N, 11.96; S, 13.69; Found C, 36.12; H, 4.08; N, 11.89; S, 13.45.

The complex $[\mathbf{Mo_2O_2S_2(L^7)}]$ is more soluble than the analogue $[\mathbf{Mo_2O_2S_2(L^6)}]$. A powder was obtained after few days of slow evaporation and characterized by ^1H NMR (see Fig. S1B, ESI†) revealing a complicated spectrum which probably corresponds to a mixture of isomers of $[\mathbf{Mo_2O_2S_2(L^7)}]$ with some partial decoordination of the ligand. In a previous paper, we evidenced that playing on the "aldehyde part" of the thiosemicarbazone ligand can influence the coordination mode of the ligand and lead to a mixture up to 8 isomers in some cases.[20] With the nitro group, the reactivity of the ligand with the thiocation seems affected and the complex we obtain appears poorly stable in solution. However, ESI-MS spectrum (Fig. S2†) performed in negative mode in DMSO/MeOH (5/95) mixture revealed peaks mainly assigned to the expected formula of the complex as mono and dianionic species associated with some

molecules of solvents probably coordinated to the Mo atoms. Finally, the cyclovoltammetry studies in solution surprisingly lead to well-defined reduction waves, which suggest $[\mathbf{Mo_2O_2S_2(L^7)}]$ is stable under these conditions of ionic strength. This result prompted us to use this complex and further evaluate its HER activity.

Results and discussion

Evidence of HER for Mo-complexes

The complexes, dispersed in a mixture of vulcanised carbon and of Nafion polymer, were physisorbed by drop casting at the surface of a carbon electrode as described in the Experimental section (ESI†). Fig. 2 shows SEM micrographs of the resulting structures for the modified electrode obtained with complex $[\mathbf{Mo_2O_2S_2(L^1)}]$ and the corresponding chemical microanalyses performed by EDS. The structure of the deposit is very similar to that previously obtained by Al Cheikh *et al.* with the complex $[\mathbf{Mo_3S_4Pd(H_2O)_3(acacbutyl)_3}]^{+}$.[15] It shows carbon particles with lot of defaults and pores at the surface. EDS spectrum (Fig. 2b) revealed the presence of F, Mo and S atoms respectively corresponding to the Nafion polymer and to the complex, as expected, while Fig. 2c evidences that the Mo complex is homogeneously dispersed over the whole surface of the electrode (pink dots).

The HER activity of the complexes $[\mathbf{Mo_2O_2S_2(L^1)}]$, $[\mathbf{Mo_2O_2S_2(L^2)}]$, $[(\mathbf{Mo_2O_2S_2})_2(\mathbf{L^3})_2]$, $[(\mathbf{Mo_2O_2S_2})_2(\mathbf{L^4})_2]$, and $[(\mathbf{Mo_2O_2S_2})_2(\mathbf{L^5})_2]$ was evaluated by Linear Sweep Voltammetry (LSV) on modified electrodes in an aqueous HCl/NaCl medium between pH = 7 and pH = 1 (Fig. 3 and Fig. S3, ESI†).

In all cases, the voltammograms show HER activity increasing with decreasing pH. An example is given in Fig. 3A for $[\mathbf{Mo_2O_2S_2(L^1)}]$, while the other LSV curves are shown in Fig. S3 (ESI†). Between pH = 7 and pH = 4, no electrochemical response is observed. From pH = 3, a cathodic current appears and further increases as the pH decreases, typical of the reduction of protons to hydrogen. At pH = 1, the start of catalysis is observed at $E_{\text{onset}} = -0.3$ V *vs.* NHE for $[\mathbf{Mo_2O_2S_2(L^1)}]$. The variation in current density as a function of potential (Fig. 3B) is comparable to those obtained for $[\mathrm{Mo_3S_4}]^{4+}$ complexes ($E_{\text{onset}} = -0.2$ V *vs.* NHE at pH = 0.4) deposited on different substrates for which hydrogen formation has been demonstrated.[14,15] The behaviour of the other complexes is similar with comparable E_{onset} values (see Fig. S3, ESI†), suggesting that the ligand and the nuclearity of the complexes have little influence on the HER process, in contrast with properties of $Mo_2O_2S_2$-based hybrid rings[12] and in contrast with work of Orio and coworkers on Ni and Co-thiosemicarbazone complexes.[25,28,29] Nevertheless, the cathodic current values achieved are significantly lower than those measured for $[\mathbf{Mo_2O_2S_2(L^1)}]$, which appears to be the most efficient in this series.

Hydrogen formation was confirmed by gas chromatography (GC) during electrolysis at $E = -0.4$ V *vs.* NHE for 15 hours and a TOF value of 8×10^{-5} s^{-1} has been calculated showing a low activity of $[\mathbf{Mo_2O_2S_2(L^1)}]$ compared to cluster $[\mathrm{Mo_3S_4}]^{4+}$ deposited on HOPG.[14] Despite its moderate catalytic properties, $[\mathbf{Mo_2O_2S_2(L^1)}]$ displays a high faradaic efficiency of 94%, while 80–88% faradaic yields were recently reported for Co and Ni-thiosemicarbazone complexes in solution in acetonitrile.[25]

Current variations measured at $E = -0.4$ V *vs.* NHE at different scan rates between 50 and 300 mV s^{-1} and in the pH range between 6 and 2 (Fig. S4, ESI†) show a linear dependence of current with scan rate. This result is consistent with a surface redox process with rapid material transport in the film and not a solution process.[43–45] Furthermore, an XPS study demonstrates that the complex $[\mathbf{Mo_2O_2S_2(L^1)}]$ deposited on the electrode surface corresponds to the initial crude complex and that the complex remained confined at the surface even after 15 hours of electrolysis (Fig. 4).

More in details, Fig. 4a shows the Mo 3d (bottom) and S 2p (top) core levels recorded by XPS on the complex $[\mathbf{Mo_2O_2S_2(L^1)}]$ in powder form. The S 2p spectral region is composed of a single doublet (S 2p$_{3/2}$ and S 2p$_{1/2}$ centered at 162.4 and 163.7 eV, respectively) associated with S^{2-} species. It is worth noting that Mo 3d core level is known to overlap with the S 2s one. Therefore, the contribution of S^{2-} species is found at 226.7 eV in the Mo 3d window. The signal is complemented by a doublet detected at 230.8 eV with a spin–orbit splitting of 3.2 eV, which corresponds to the +V oxidation state. These results are consistent with the structure of the $[\mathbf{Mo_2O_2S_2(L^1)}]$
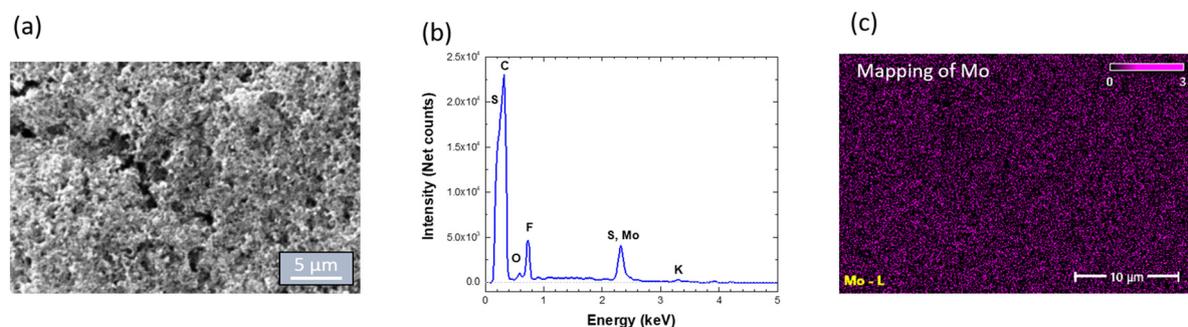
Fig. 2 (a) SEM image at 5 μm scale of an electrode modified with complex $[\mathbf{Mo_2O_2S_2(L^1)}]$ (×12 000); (b) EDS spectrum of the deposit (c) dot map for Mo element in the deposit.

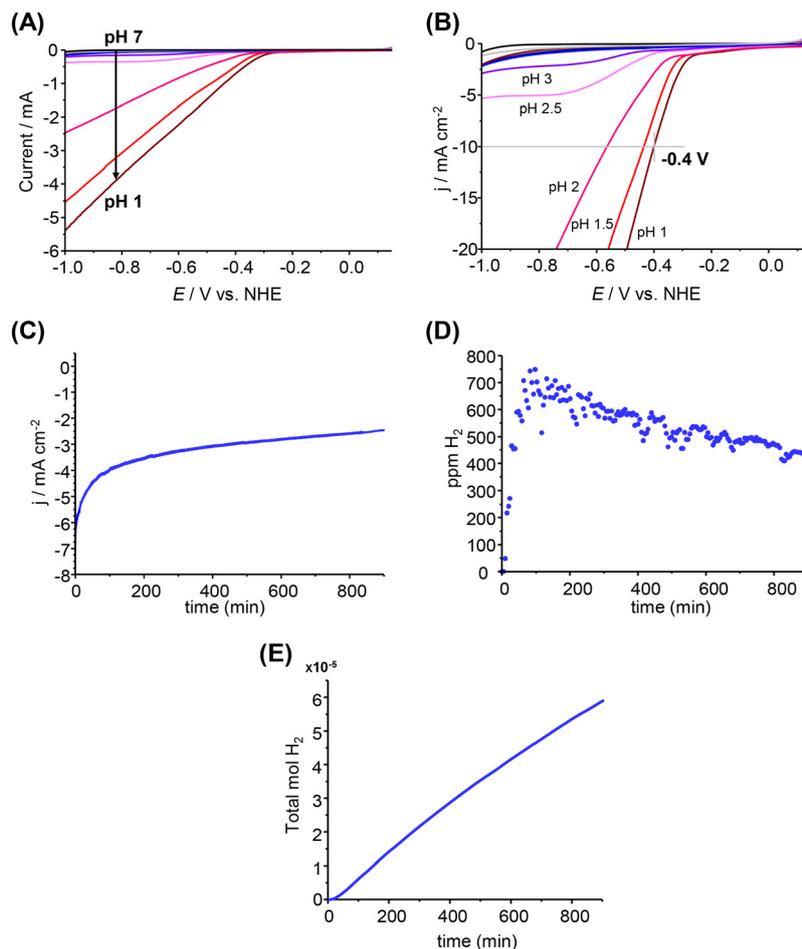**Fig. 3** (A) LSV curves recorded on modified glassy carbon electrode for [$Mo_2O_2S_2(L^1)$] from pH = 7 to pH = 1 in HCl/NaCl solutions at 50 mV s^{-1} scan rate; (B) overpotential at current density −10 mA cm^{-2} chosen for the chronoamperometry measurements; (C) chronoamperometry over 15 h for [$Mo_2O_2S_2(L^1)$] complex; (D) hydrogen monitoring by gas chromatography and (E) total amount of hydrogen produced during chronoamperometry.

complex. Note that an additional doublet at lower binding energy (229.0 eV) is also visible and is attributed to a reduced state of Mo (Mo(+IV)), a phenomenon which can be due to X-ray exposure of the complex.

The analysis of the catalytic ink at the surface of a glassy carbon electrode before catalysis (Fig. 4b) evidenced the same chemical environments as the ones previously described, which confirms the presence of the complex in the composite. Nevertheless, two new contributions were observed at high binding energy in the S 2p and Mo 3d spectral region. The broad doublet at 168.3 eV in the S 2p high resolution spectrum is typical of the sulfonates group originating from the Nafion used to prepare the catalytic ink. While in the case of the Mo 3d, a third doublet at 232.1 eV is necessary to properly reconstruct the experimental data. It corresponds to an oxidized state of Mo (Mo^{+VI}). Although the intensity of this new Mo contribution is low, its presence means that the compound was slightly oxidized during ink manufacturing or it is simply native oxidation of the surface since no particular precautions (inert atmosphere) were paid for the storage of the samples

before analysis. Finally, the same spectral regions were evaluated after HER (Fig. 4c). The Mo 3d signal is similar to the one obtained before HER in term of intensity and chemical environments. This demonstrate a certain stability of the compound upon catalysis even at pH = 1 in contrast with almost all oxothiomolybdenum rings previously studied for HER which decomposes at low pH.[12] From the S 2p point of view, an extra contribution is needed to reconstruct the spectrum. This new doublet at 163.2 V with 1.1 eV spin–orbit splitting can be interpreted as the presence of S(−I) species at the surface. So, sulfur would tend to partially oxidize during HER process.

Influence of donating or withdrawing substituents on HER properties

The first series of complexes [$Mo_2O_2S_2(L^n)_m$] (n = 1 to 5, m = 1 or 2) showed no significant difference in HER properties, and the [$Mo_2O_2S_2(L^1)$] complex proved to be the most efficient of this series. In a second step, we wanted to determine how the introduction of methoxy donor groups ([$Mo_2O_2S_2(L^6)$]
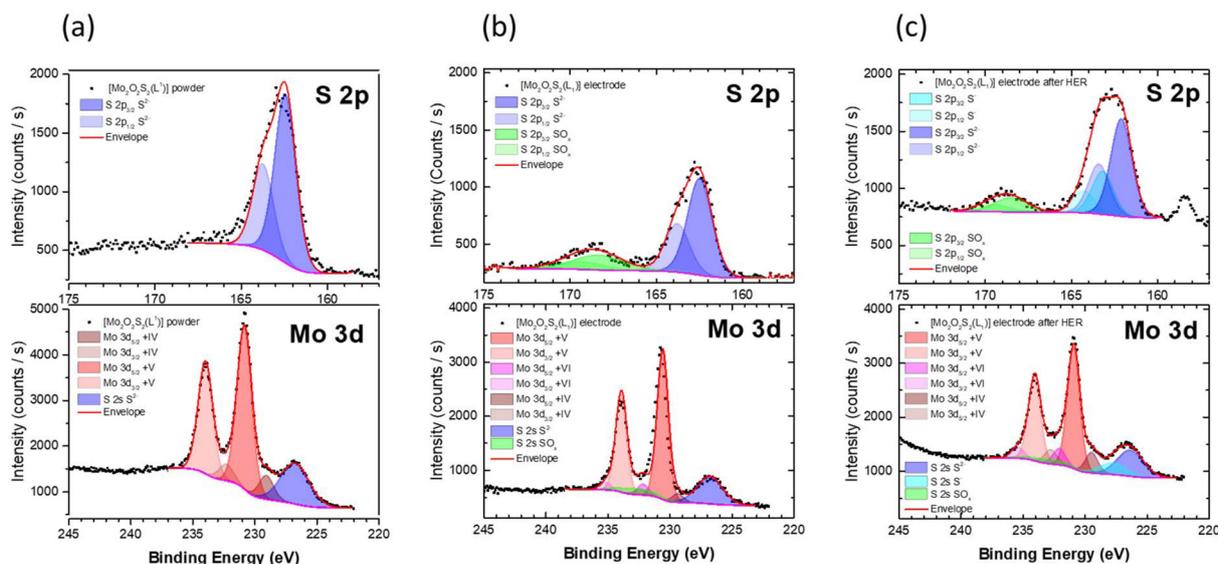
Fig. 4 Mo 3d and S 2p XPS spectra of the Mo complex [**Mo$_2$O$_2$S$_2$(L^1)**] and associated reconstruction in powder form (a) and as an active material in the catalytic ink before (b) and after HER process (c).

complex) or nitro attracting groups ([**Mo$_2$O$_2$S$_2$(L^7)**] complex) on the ligand can influence the properties of the complexes. Indeed, Orio and coworkers demonstrated that the electrochemical, electrocatalytic and photocatalytic behaviours of Ni and Co-thiosemicarbazone complexes can be modulated by introduction of various substituents of the ligand.[26,29] A preliminary DFT study was then carried out to verify this hypothesis in the case of Mo$_2$O$_2$S$_2$-based complexes.

For the three complexes analyzed, we examined the frontier orbitals and the Molecular Electrostatic Potential (MEP). Fig. 5 presents the HOMO and LUMO orbitals, along with the MEP from two perspectives: front and side views. Additionally, selected geometric parameters are illustrated schematically in Fig. 6. A comprehensive summary of all geometric and electronic parameters is provided in Table 1, including the distance between the two benzene rings ($d_{\varnothing-\varnothing}$), the molyb-
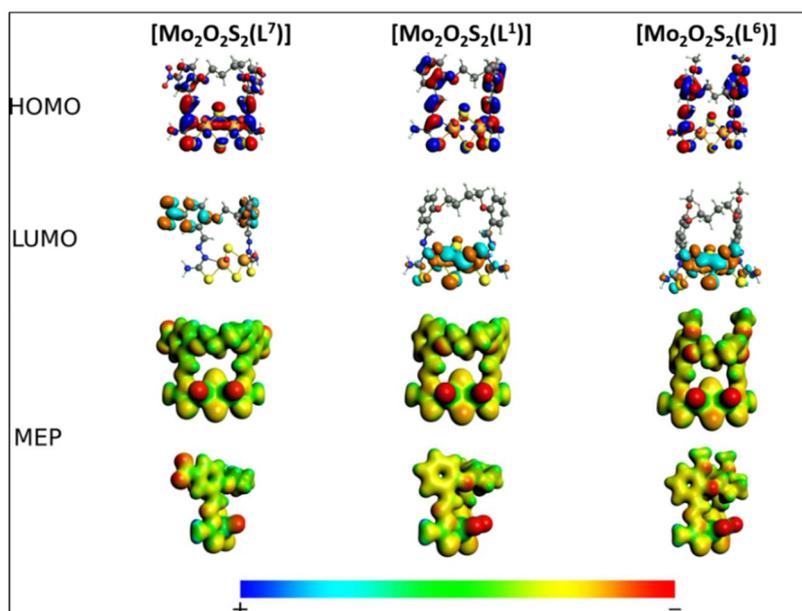
Fig. 5 HOMO, LUMO and electrostatic potential mapped on an electron density iso-surface for considered complexes [**Mo$_2$O$_2$S$_2$(L^1)**], [**Mo$_2$O$_2$S$_2$(L^6)**] (−OMe substituents) and [**Mo$_2$O$_2$S$_2$(L^7)**] (−NO$_2$ substituents). Complexes are classified in columns. The values for the MEPs go from +0.47 to −0.069 au.

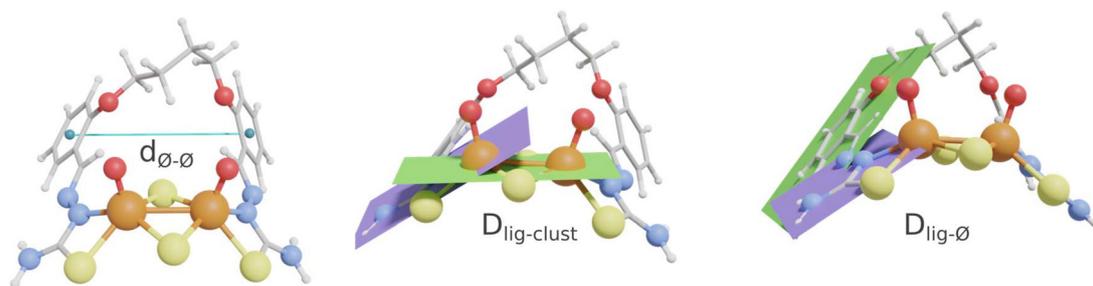**Fig. 6** Visual representation of non-trivial geometric parameters for **Mo₂O₂S₂(L^1,7,6)**. Left: distance between the two aromatic rings; center: dihedral angle between the metals and the ligand; right: dihedral angle between the aromatic ring and the ligand.

Table 1 Geometric and electronic parameters calculated for complexes [Mo₂O₂S₂(L¹)], [Mo₂O₂S₂(L⁶)], and [Mo₂O₂S₂(L⁷)]. X-Ray data are given into brackets for complexes [Mo₂O₂S₂(L¹)] and [Mo₂O₂S₂(L⁶)] for comparison

		[Mo₂O₂S₂(L⁷)] (−NO₂)	[Mo₂O₂S₂(L¹)]	[Mo₂O₂S₂(L⁶)] (−OMe)
$d_{\varnothing-\varnothing}$ (Å)		7.56	7.30	6.25
d_{Mo-Mo} (Å)		2.85	2.85 (2.85)	2.85 (2.84)
d_{Mo-N} (Å)		2.175	2.175 (2.13)	2.16 (2.15)
d_{Mo-S} (Å)		2.49 (2.49 for Mo−S$_{ligand}$; 2.34 for Mo−S$_{bridge}$)	2.49 (2.49 for Mo−S$_{ligand}$; 2.34 for Mo−S$_{bridge}$)	2.49 (2.49 for Mo−S$_{ligand}$; 2.34 for Mo−S$_{bridge}$)
$D_{lig-\varnothing}$ (°)		5–10	5–10	10–20
$D_{clust-lig}$ (°)		10–15	10–15	15–20
MDC-m	q_C	0.145/0.149	0.143/0.148	0.141/0.149
	q_N	−0.177/−0.169	−0.191/−0.184	−0.192/−0.193
	$q_{N(Mo)}$	−0.461/−0.458	−0.466/−0.464	−0.470/−0.472
HOMO (eV)		−5.634	−5.403	−5.429
LUMO (eV)		−3.761	−3.153	−3.120
H–L gap (eV)		1.873	2.250	2.309

denum–molybdenum distance, frontier orbital energies, and Multipolar Derived Charges (MDC).

The first observation from the data in Fig. 5 and Table 1 is the progressive separation of the two benzene rings ($d_{\varnothing-\varnothing}$ (Å)) as electronic density decreases. Adding an electron withdrawing group like −NO₂ (−I and −R effect) turned into a separation of the opposite benzene rings. On the other hand, introducing an electron donor group like −OCH₃ (−I and +R effect) turned into an approximation of those and a more negative surface. Also, the inclination of the benzene rings changes about the thiosemicarbazone. In Table 1 we can see how the dihedral angle of the ligand and the benzene rings $D_{lig-\varnothing}$ (°) are tilted from 5 to 10 degrees from the complete planarity of the ligand for the electron impoverished rings, while for the electron enriched ring, this angle tilts from 10 to 20 degrees.

These modifications are mainly localised on the aromatic rings of the ligands and do not seem to affect the environment around the Mo atoms. The Mo coordination spheres stays unaffected by these substituent effects and the mapped electrostatic potentials are not significantly modified around the [Mo₂O₂S₂]²⁺ cluster. In contrast, in terms of frontier orbitals of the three studied complexes, there is a reversal of the

HOMO and the LUMO orbitals of the nitro-compound respect the other two complexes. Indeed, for the nitro compound the LUMO is localised on the ligand, while the LUMO is localised on the [Mo₂O₂S₂]²⁺ cluster for the two others for which the HOMO–LUMO gap is slightly higher upon addition of methoxy groups on the ligand (see Fig. 5). From these results, we decided to synthesize the two complexes [Mo₂O₂S₂(L⁶)] and [Mo₂O₂S₂(L⁷)].

The former, [Mo₂O₂S₂(L⁶)], was obtained as single crystals. It crystallizes in the $C_{2/c}$ space group. The crystallographic data are gathered in Tables S1 and S2 (ESI†) and the molecular structure of the complex depicted in Fig. 7A is very similar to those reported for [Mo₂O₂S₂(L¹)] and [Mo₂O₂S₂(L²)].²³ In addition, the ¹H NMR spectra of [Mo₂O₂S₂(L⁶)] (Fig. 7C) perfectly agrees for the formation of the complex and the maintain of the structure in solution.

Concerning [Mo₂O₂S₂(L⁷)], the synthesis revealed to be more complicated with a poorly stable complex in solution and probably a mixture of isomers (Fig. S1B, ESI†).

Nonetheless, cyclic voltammograms of the three compounds [Mo₂O₂S₂(L¹)], [Mo₂O₂S₂(L⁶)], and [Mo₂O₂S₂(L⁷)] at 0.5×10^{-3} mol L⁻¹ concentration, were recorded in 0.1 mol L⁻¹ Bu₄NPF₆–DMF electrolyte at $\nu = 0.1$ V s⁻¹ (Fig. 8A, B and S5,† respectively).

[Mo₂O₂S₂(L¹)] and [Mo₂O₂S₂(L⁶)] display a partially-reversible reduction process at $E_{1/2}^{red1} = -1.234$ and -1.405 V vs. NHE respectively (see Fig. 8 and Table 2). As demonstrated by previous electrochemical studies of {Mo₂S₂O₂}-complexes in organic medium,⁴⁶,⁴⁷ the reduction processes of [Mo₂O₂S₂(L¹)] and [Mo₂O₂S₂(L⁶)] are assigned to be monoelectronic and localised on Mo(v) atoms according to DFT calculations and the nature of LUMO frontier orbital. The second irreversible reduction processes of [Mo₂O₂S₂(L¹)] and [Mo₂O₂S₂(L⁶)] respectively at $E_{p_c}^{red2} = -1.606$ and -1.632 V are also monoelectronic (current peak ratios $I_{p_c}^{red2}/I_{p_c}^{red1} = 0.9$ and 1.0).

[Mo₂O₂S₂(L⁷)] (Fig. S5†) undergoes an irreversible reduction process at $E_{p_c}^{red1} = -0.940$ V corresponding to the reduction of the two nitro-/−NO₂ substituents of the thiosemicarbazone ligand⁴⁸ followed by a second partially-reversible reduction process at $E_{p_c}^{red2} = -1.043$ V. This is perfectly in line with DFT calculation evidencing the LUMO localised on the nitro groups.
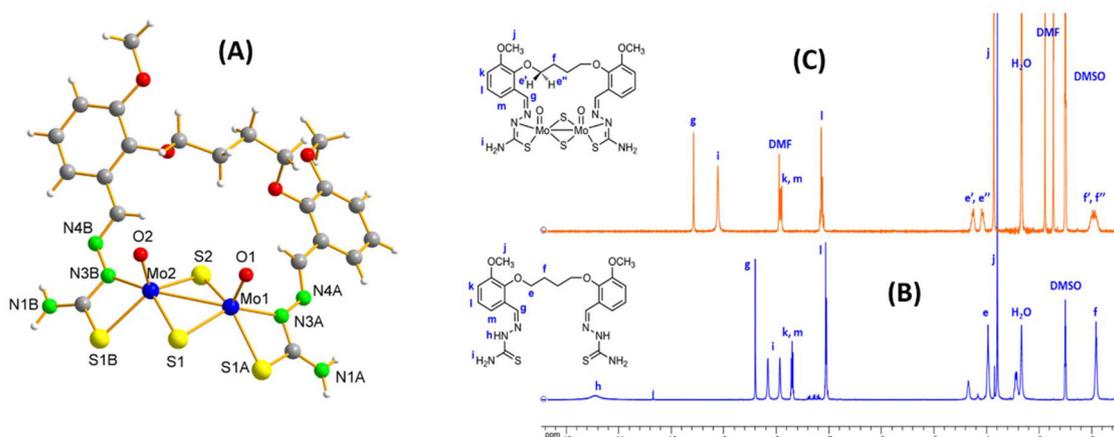
Fig. 7 (A) X-ray molecular structure of complex [$Mo_2O_2S_2(L^6)$]; ^1H NMR spectra of ligand H_2L^6 (B) and complex [$Mo_2O_2S_2(L^6)$] (C) in DMSO.
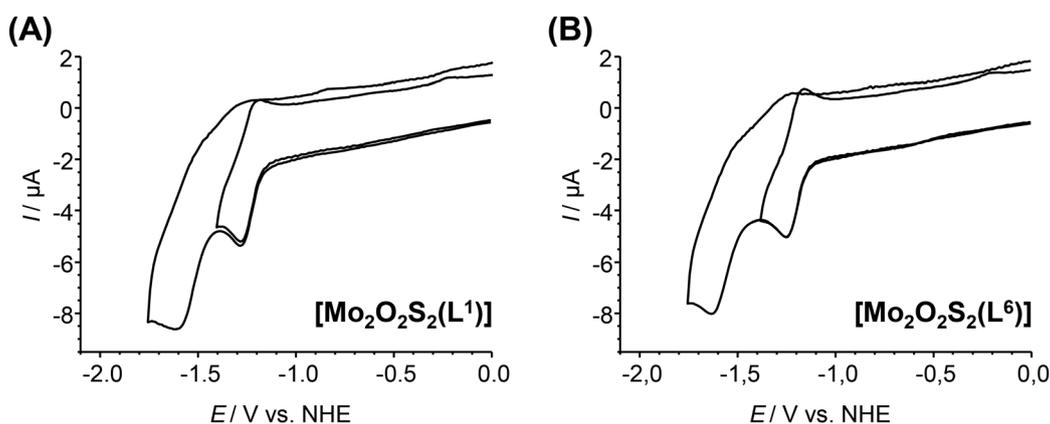
Fig. 8 Cyclic voltammograms of [$Mo_2O_2S_2(L^1)$] (A), [$Mo_2O_2S_2(L^6)$] (B) and [$Mo_2O_2S_2(L^7)$] (C) (0.5×10^{-3} mol L^{-1}) in 0.1 mol L^{-1} Bu_4NPF_6–DMF solution at $\nu = 0.1$ V s^{-1}.

Table 2 Electrochemical data of [$Mo_2O_2S_2$-L^1], [$Mo_2O_2S_2$-L^6] and [$Mo_2O_2S_2$-L^7]. Potentials are referred towards NHE in 0.1 mol L^{-1} Bu_4NPF_6–DMF solution at $\nu = 0.1$ V s^{-1}. Ip_c^{red1}/Ip_c^{red2} were determined by using the Nicholson method[49]

	Ep_c^{red1}	Ep_a^{red1}	$E_{1/2}$	ΔE	Ip_a^{red1}/Ip_c^{red1}	Ep_c^{red2}	Ip_c^{red1}/Ip_c^{red2}
[$Mo_2O_2S_2(L^1)$]	−1.279	−1.189	**−1.234**	0.090	0.58	−1.606	0.90
[$Mo_2O_2S_2(L^6)$]	−1.251	−1.165	**−1.208**	0.086	0.63	−1.632	1.01
[$Mo_2O_2S_2(L^7)$]	**−0.940**	—	—	—	—	−1.043	—

In terms of HER properties, the three complexes were compared as modified electrode by LSV method. The results are shown in Fig. S6 (ESI†). The complex [$Mo_2O_2S_2(L^6)$] appears less efficient to [$Mo_2O_2S_2(L^1)$] but similar to the activity of the previous complexes. In contrast, the complex [$Mo_2O_2S_2(L^7)$] with nitro groups appears almost not active for HER, which suggest that the HER activity probably necessitates the reduction of the Mo(v) atoms to occur. The XPS spectra performed on [$Mo_2O_2S_2(L^6)$] as powder or deposited on electrodes before catalysis (Fig. S7, ESI†) are very similar and consistent to those obtained for the complex [$Mo_2O_2S_2(L^1)$] (Fig. 4). After HER, XPS spectra evidenced that the intensity of the sulfonates

group is not impacted which is means that Nafion contained in the deposit is unaffected by the electrochemical treatment. However, the signals originating from the Mo complex [$Mo_2O_2S_2(L^6)$] are highly decreased after HER process. Even if the chemical environments detected are the same as the complex with ligand L^1, the intensity drop of both the different oxidation states of Mo and the S^{2-} contributions demonstrate the catalyst degradation during the HER process. Based on the texture of the deposit (see Fig. 2a), it is likely that parts of this deposit will detach during the process. Nafion-embedded [$Mo_2O_2S_2(L^6)$] is not stable, on the contrary of [$Mo_2O_2S_2(L^1)$].

Mechanistic studies

Among the 7 complexes tested towards HER, the complex $[\textbf{Mo}_2\textbf{O}_2\textbf{S}_2(\textbf{L}^1)]$ appears as the most efficient and DFT calculation are thus focused on this complex to establish the mechanism involved for HER process. First elements of mechanism are provided by Tafel plots carried out for the complexes by the treatment of the LSV curves at pH = 1 (Fig. 9). Usually, the efficiency of the HER process is correlated with the slope of the Tafel plot. Lower the slope, higher the efficiency. Miras *et al.* studied the HER properties for complexes $[\text{Mo}_2\text{O}_2\text{S}_2(\text{S}_2)_2]^{2-}$, $[\text{Mo}_2\text{O}_2\text{S}_2(\text{S}_2)(\text{S}_4)]^{2-}$ and $[\text{W}_2\text{O}_2\text{S}_2(\text{S}_2)(\text{S}_4)]^{2-}$ in similar conditions than ours.[19] A slope of 52–55 mV dec^{-1} was found for the two molybdenum complexes which revealed to be excellent electrocatalysts, while the tungstic analogue displaying a Tafel slope of 100 mV dec^{-1} was found less efficient for HER process compared to the two Mo analogues. In our case, for all complexes the Tafel slopes are similar and found in the range 111–135 mV dec^{-1}. These values are similar to those found for other $[\text{Mo}_3\text{S}_4]$-based complexes deposited on various surfaces[15] and typical of a diffusion-controlled reaction (typically between 120 and 240 mV per decade). In this case the limiting step of the mechanism is likely the transport of protons to the electrode surface. Interestingly, the higher Tafel's slope of the complex $[\textbf{Mo}_2\textbf{O}_2\textbf{S}_2(\textbf{L}^7)]$, in agreement with electrochemical processes, concludes a lower catalytic efficiency than the other compounds of the series.

For such a reaction and from previous studies reported for $[\text{Mo}_2\text{O}_2\text{S}_2]$-based cycles and the fact that the close environment of the Mo atoms contains several O, N, and S atoms capable of being protonated, the intramolecular Volmer–Tafel mechanism depicted in Fig. 10, is preferentially considered.

The mechanism starts with reduction of the initial complex $[\textbf{Mo}_2\textbf{O}_2\textbf{S}_2(\textbf{L}^1)]$ with two consecutive electrons leading to the anionic complexes $[\textbf{Mo}_2\textbf{O}_2\textbf{S}_2(\textbf{L}^1)]^-$ and $[\textbf{Mo}_2\textbf{O}_2\textbf{S}_2(\textbf{L}^1)]^{2-}$, as suggested by the mechanism proposed by Miras *et al.* on $[\text{Mo}_2\text{O}_2\text{S}_2(\text{S}_2)(\text{S}_x)]^{2-}$ complexes.[19] The reduction potentials referred to the NHE have been calculated as depicted in eqn (1) and (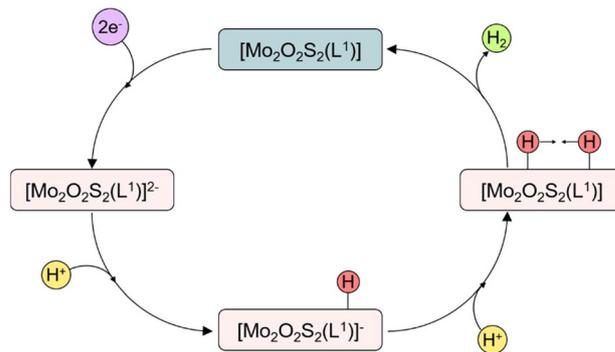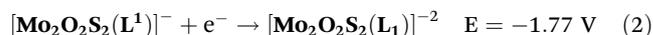2) and are in rather good agreement with the experimental values determined in DMF: $E_{1/2}^{\text{red1}}$ = −1.23 V/NHE and E_c^{red2} = −1.61 V/NHE (see Table 2), which validates the theoretical model used.

$$[\textbf{Mo}_2\textbf{O}_2\textbf{S}_2(\textbf{L}^1)] + e^- \rightarrow [\textbf{Mo}_2\textbf{O}_2\textbf{S}_2(\textbf{L}_1)]^- \quad E = -1.18 \text{ V} \quad (1)$$

$$[\textbf{Mo}_2\textbf{O}_2\textbf{S}_2(\textbf{L}^1)]^- + e^- \rightarrow [\textbf{Mo}_2\textbf{O}_2\textbf{S}_2(\textbf{L}_1)]^{-2} \quad E = -1.77 \text{ V} \quad (2)$$

The mechanism follows with two consecutive protonations of the complex. HOMO and LUMO orbitals as well as the Molecular Electrostatic Potentials (MEP) are depicted in Fig. 11. In this figure, it is possible to observe how the consecutive reductions of the initial complex mostly affect the metal region of the molecule. From both the HOMO orbitals and the MEP it is possible to see how the electrons are placed in between the two molybdenum atoms. This information is key to understand the reaction's mechanism.

Protonation plays a fundamental role in understanding reaction intermediates in hydrogen evolution reactions. Proton transfer steps influence both the mechanism and the efficiency of HER. Analysis of the calculated Molecular Electrostatic Potentials (MEPs) revealed the most basic sites which are preferred for protonation due to their higher proton affinity. All proposed protonation states were computationally modeled, and their geometries were fully optimized. The structures of the resulting monoprotonated complexes are presented in Fig. 12. Given the molecular symmetry, only half of these positions (specifically, those on the left side of the Mo–Mo core) were considered, as the equivalent positions on the opposite side would exhibit identical behavior. The selected protonation sites include the terminal Mo=O oxygen, the bridging sulfur atoms (labelled as S_2A and S_2B), and the coordinating nitrogen and sulfur atoms from the thiosemicarbazone ligand. Additionally, the molybdenum (Mo) center was considered as a potential protonation site, as its protonation could lead to the formation of a molybdenum hydride adduct, which may exist as either a formally Mo(III) intermediate or two Mo(IV) centers through intramolecular electron transfer with the Mo(V) oxidation state. This transformation is of particular
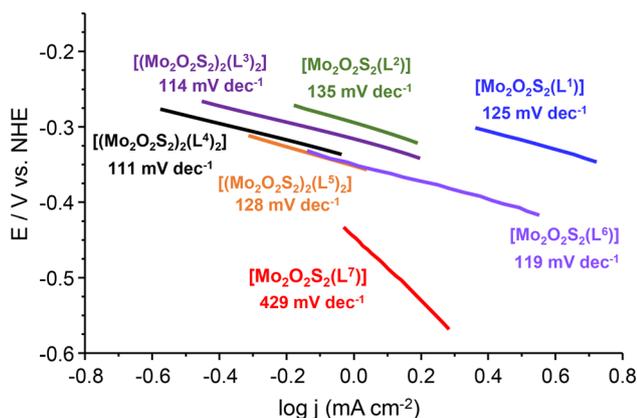

Fig. 10 Volmer–Tafel mechanism considered for hydrogen evolution reaction (HER).

Fig. 9 HER Tafel plots from LSV curves at pH = 1 for complexes.

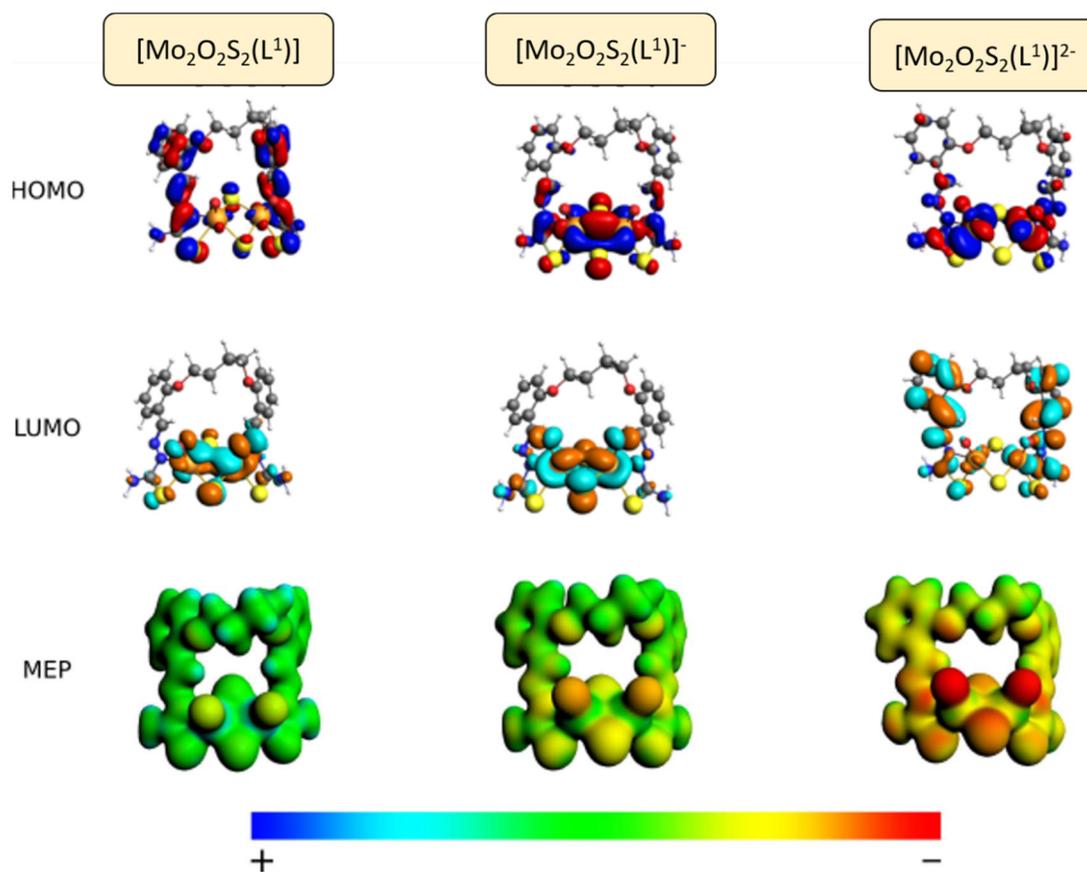**Fig. 11** Frontier orbitals and molecular electrostatic potential for the [$Mo_2O_2S_2(L^1)$] complex and its reduction derivatives (1 and 2 electrons). MEP values go from +0.46 to −0.33 au.
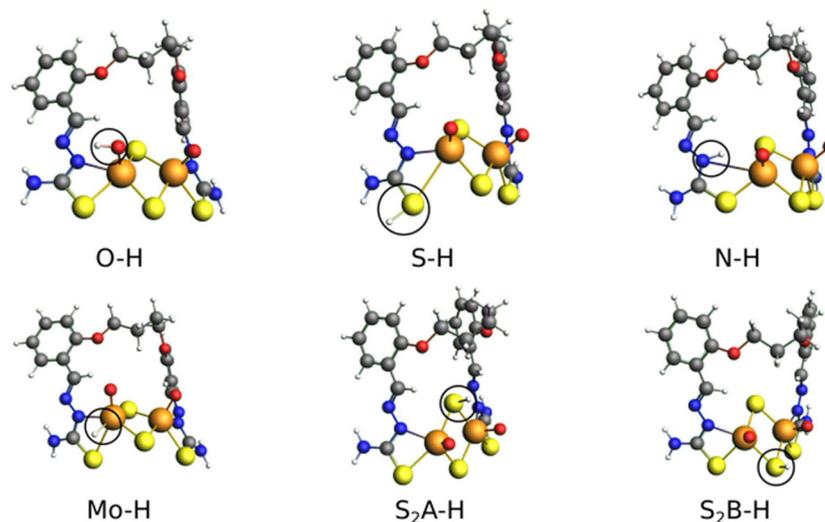

Fig. 12 Molecular views of the different hypotheses of 2 electrons reduced mono-protonated complexes. The protonation site is marked with a black circle around it.

interest due to its potential role in facilitating H–H bond formation in subsequent stages of the reaction mechanism.

Table 3 summarizes the electronic energies of both monoprotonated and diprotonated complexes. The first column presents the monoprotonated complexes, specifying the protonation site and its corresponding energy. From these calculations, we extracted the electronic energies and selected the three monoprotonated complexes with the lowest energy values (N–H, O–H, Mo–H). The three lowest-energy monoprotonated complexes were further protonated at the remaining preselected sites obtaining diprotonated complexes.

Among the diprotonated complexes, only three have hydrogen atoms positioned closely enough to facilitate the hydrogen formation reaction (in bold in the Table 3): OH–SH, OH–MoH, and MoH–SH. The reaction pathways for hydrogen evolution were analyzed by optimizing the transition state structures and performing an Intrinsic Reaction Coordinate (IRC) analysis (see Fig. 13A). The transition states (TS) are labeled according to the two protonation sites involved. The geometries of the transition states are depicted in Fig. 14a, b and c, respectively. The H–H distances are depicted in each of the figures.

For a better understanding of the mechanistic pathway of the HER an energy profile is plotted to compare the performance of the three reaction pathways (Fig. 13B). We took the two-electron reduced unprotonated complex and 2 molecules of the Zundel cation ($[H_5O_2]^+$) as reference. The first step consists of the first protonation of the reduced complex. For this step only two possibilities were considered: the protonation of the terminal oxygen (OH, red and yellow) and the molybdenum hydride formation (MoH, green). For this step there is a huge energy difference between the two pathways (around 20 kcal mol^{-1}) in favour of the formation of Mo-hydride moiety.

The second step of the mechanistic pathway consists of the second protonation of the complexes. For the OH step, there is a bifurcation between the yellow and red lines as two different protonations were considered from the first step. The formation of the molybdenum hydride (OH–MoH, yellow
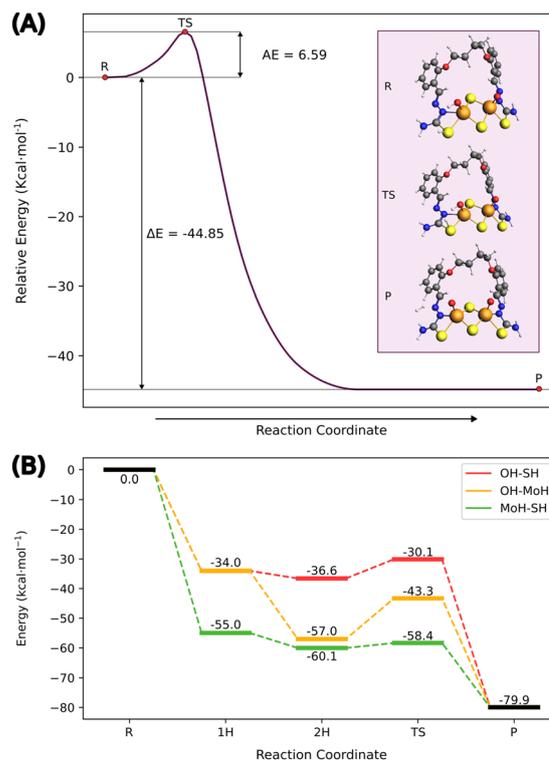

Fig. 13 (A) Representation of the Intrinsic Reaction Coordinate (IRC) for $TS_{OH–SH}$; (B) energy profile for the consecutive protonations of the 2-electron reduced complex towards the H_2 formation. Energies in kcal mol^{-1}.

pathway) implies a high stabilization in comparison to the protonation of the thiosemicarbazone sulfur atom (OH–SH, red pathway). At this point a general trend can be seen: the formation of the Mo-hydride is more energetically favoured than the protonations. Such an assumption is supported by several other works showing the existence of {Mo–H} entities, especially Mo(IV)–H, within various Mo–S molecular combinations[50–55] and work of Orio and coworkers who recently evidenced a similar formation of metal-hydride moiety in a cobalt-thiosemicarbazone complex during the HER process after the reduction of the Co(+II) center.[25]

The Transition States (TS) found across this mechanism differ in energy between them. The second step of the green pathway (Fig. 14c MoH–SH) implies the protonation and thus decoordination of the thiolate group of the thiosemicarbazone ligand with an energy gain of 5 kcal mol^{-1}. An energy difference between the 2-protons intermediate and the TS (MoH–SH) is of 2 kcal mol^{-1}, making the process nearly barrierless to achieve the HER process by combining the sulfur SH proton with the hydride to give dihydrogen and regenerate the Mo(v) atoms. Moreover, the red OH–SH and yellow pathways OH–MoH have a higher energy barrier, 6 (OH–SH) and 14 (OH–MoH) kcal mol^{-1} respectively, but all pathways remain feasible at room temperature. Hence the DFT study not only proposes the plausible reaction mechanism but also supports the

Table 3 Protonated complexes relative bonding energy in kcal mol^{-1}

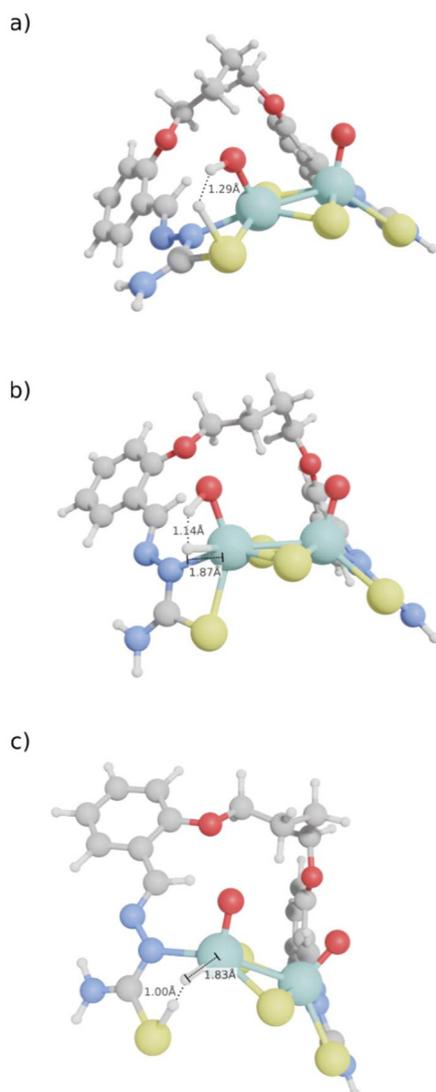|	1st proton		2nd proton	
	Site	Energy	Site	Energy
$[Mo_2O_2S_2\text{-}L_6]^{2-}$	N–H	−39.6	S–H	−38.1
			S_2A-H	−49.9
			O–H	−47.3
			Mo–H	−67.5
	O–H	−34.0	**S–H (TS$_{OH–SH}$)**	**−36.6**
			N–H	−58.2
			Mo–H (TS$_{OH–MoH}$)	**−57.1**
	Mo–H	−55.0	N–H	−58.8
			S–H (TS$_{MoH–SH}$)	**−60.1**
			S_2B-H	−48.6
			O–H	−57.1
	S–H	−22.8		
	S_2A-H	−23.5		
	S_2B-H	−31.3		

Fig. 14 (A) Close-up view of the geometry of TS_{OH-SH}. H−H distance is shown in angstroms (1.287 Å); (B) close-up view of the geometry of TS_{OH-MoH}. H−H and H−Mo distances are shown in angstroms (1.137 and 1.872 Å, respectively); (C) close-up view of the geometry of TS_{MoH-SH} involving the decoordination of the thiolate group of the thiosemicarbazone ligand. H−H and H−Mo distances are shown in angstroms (1.003 and 1.834 Å, respectively).

thermodynamic feasibility of the overall process under experimental acidic conditions. Unfortunately, we did not succeed to evidence by ^{1}H or ^{15}N NMR the protonation of the ligand nor the formation of the Mo−H moiety but the proposed mechanism agree well with our data acquired and the proposed mechanism for HER with oxothiomolybdenum rings.[12] Nevertheless it contrast with the HER mechanism proposed for $[Mo_2O_2S_2(S_2)(S_x)]^{2-}$ complexes in which, after two electrons reduction on Mo(+v) centers, the structure reorganize to break and reduce a disulfide ligand S_2^{2-} into two sulfide groups S^{2-}, which are then protonated and combined with Zundel cation to give H_2.[19]

Conclusion

In this study, we demonstrated that a family of complexes formed between the thiocation $[Mo_2O_2S_2]^{2+}$ and bis-thiosemi-carbazone ligands are electro-active for the reduction of protons to hydrogen in the form of modified electrodes and in aqueous media up to pH = 1. One of the complexes, the simplest, $[\mathbf{Mo_2O_2S_2(L^1)}]$ proved to be the most active and the most robust in terms of stability but the efficiency appears comparable to previous molybdenum cyclic systems and much less efficient than $[Mo_2O_2S_2(S_2)(S_x)]^{2-}$ complexes. DFT studies considered a Volmer–Tafel mechanism involving a first step of reduction of the Mo cluster to 2 electrons, a first protonation leading to the formation of a molybdenum hydride, a second protonation on the thiolate of the nearby thiosemicarbazone ligand associated with the decoordination of S and then the combination of this proton with a hydride to form H_2 and regenerate the initial complex. This mechanism agrees with our previous studies of Mo-cycles but differs from mechanisms proposed for Ni- and Co-thiosemicarbazone complexes as well as for $[Mo_2O_2S_2(S_2)(S_x)]^{2-}$ complexes. It offers a mechanistic alternative demonstrating the richness of Mo-complexes and thiosemicarbazone complexes in terms of catalytic pathways.

In this study, it was not possible to significantly modulate the HER properties of the complexes by altering the nature of the ligands. However, in terms of future prospects, we now plan to modify the environment of the complex, in particular by incorporating it into various organic and biological materials.

Author contributions

Jordi Buils: DFT calculations; Diana Cebotari, and Yasmine Bouaouni: synthesis and characterizations of complexes; Sergiu Calancea, Yasmine Bouaouni, Roa AlChamandi and Maxime Laurans: electrochemical studies; Jérome Marrot: X-ray diffraction studies: Mathieu Fregnaux: XPS studies; Mireia Segado-Centellas, Carles Bo and Sébastien Floquet: supervision of this work, funding acquisition and writing.

Data availability

Details of the synthesis, characterizations, properties measurements, are given in the ESI.† Further details can be obtained by contacting the corresponding authors.

A dataset collection with all the DFT calculations is available in the ioChem-BD repository through the following link **https://dx.doi.org/10.19061/iochem-bd-1-371**.

Conflicts of interest

There are no conflicts to declare.

References

1 T. F. Jaramillo, K. P. Jorgensen, J. Bonde, J. H. Nielsen, S. Horch and I. Chorkendorff, *Science*, 2007, **317**, 100–102.

2 H. Vrubel, D. Merki and X. L. Hu, *Energy Environ. Sci.*, 2012, **5**, 6136–6144.

3 T. Bourgeteau, D. Tondelier, B. Geffroy, R. Brisse, C. Laberty-Robert, S. Campidelli, R. de Bettignies, V. Artero, S. Palacin and B. Jousselme, *Energy Environ. Sci.*, 2013, **6**, 2706–2713.

4 I. Roger, R. Moca, H. Miras, K. Crawford, D. Moran, A. Ganin and M. Symes, *J. Mater. Chem. A*, 2017, **5**, 1472–1480.

5 R. Ye, Y. Bao, J. Huang, Y. Zhao, Z. Fan, H. Chen, X. Hu and N. Zhuang, *Catal. Lett.*, 2020, **150**, 3402–3408.

6 A. Morozan, H. Johnson, C. Roiron, G. Genay, D. Aldakov, A. Ghedjatti, C. Nguyen, P. Tran, S. Kinge and V. Artero, *ACS Catal.*, 2020, **10**, 14336–14348.

7 P. Tran, T. Tran, M. Orio, S. Torelli, Q. Truong, K. Nayuki, Y. Sasaki, S. Chiam, R. Yi, I. Honma, J. Barber and V. Artero, *Nat. Mater.*, 2016, **15**, 640–646.

8 B. Keita, S. Floquet, J.-F. Lemonnier, E. Cadot, A. Kachmar, M. Benard, M.-M. Rohmer and L. Nadjo, *J. Phys. Chem. C*, 2008, **112**, 1109–1114.

9 S. Duval, S. Floquet, C. Simonnet-Jegat, J. Marrot, R. N. Biboum, B. Keita, L. Nadjo, M. Haouas, F. Taulelle and E. Cadot, *J. Am. Chem. Soc.*, 2010, **132**, 2069–2077.

10 A. Hijazi, J. C. Kemmegne-Mbouguen, S. Floquet, J. Marrot, C. R. Mayer, V. Artero and E. Cadot, *Inorg. Chem.*, 2011, **50**, 9031–9038.

11 H. El Moll, J. C. Kemmegne-Mbouguen, M. Haouas, F. Taulelle, J. Marrot, E. Cadot, P. Mialane, S. Floquet and A. Dolbecq, *Dalton Trans.*, 2012, **41**, 9955–9963.

12 A. Hijazi, J. C. Kemmegne-Mbouguen, S. Floquet, J. Marrot, J. Fize, V. Artero, O. David, E. Magnier, B. Pegot and E. Cadot, *Dalton Trans.*, 2013, **42**, 4848–4858.

13 T. Shibahara, M. Yamasaki, G. Sakane, K. Minami, T. Yabuki and A. Ichimura, *Inorg. Chem.*, 1992, **31**, 640–647.

14 T. F. Jaramillo, J. Bonde, J. D. Zhang, B. L. Ooi, K. Andersson, J. Ulstrup and I. Chorkendorff, *J. Phys. Chem. C*, 2008, **112**, 17492–17498.

15 J. Al Cheikh, R. Zakari, A. C. Bhosale, A. Villagra, N. Leclerc, S. Floquet, P. C. Ghosh, A. Ranjbari, E. Cadot, P. Millet and L. Assaud, *Mater. Adv.*, 2020, **1**, 430–440.

16 Y. D. Hou, B. L. Abrams, P. C. K. Vesborg, M. E. Bjorketun, K. Herbst, L. Bech, A. M. Setti, C. D. Damsgaard, T. Pedersen, O. Hansen, J. Rossmeisl, S. Dahl, J. K. Norskov and I. Chorkendorff, *Nat. Mater.*, 2011, **10**, 434–438.

17 Y. Smortsova, C. Falaise, A. Fatima, M. Ha-Thi, R. Meallet-Renault, K. Steenkeste, S. Al-Bacha, T. Chaib, L. Assaud, M. Lepeltier, M. Haouas, N. Leclerc, T. Pino and E. Cadot, *Chem. – Eur. J.*, 2021, **27**, 17094–17103.

18 A. Elliott and H. Miras, *J. Coord. Chem.*, 2022, **75**, 1467–1493.

19 J. McAllister, N. Bandeira, J. McGlynn, A. Ganin, Y. Song, C. Bo and H. Miras, *Nat. Commun.*, 2019, **10**, 370.

20 A. Fuior, D. Cebotari, M. Haouas, J. Marrot, G. Espallargas, V. Guerineau, D. Touboul, R. Rusnac, A. Gulea and S. Floquet, *ACS Omega*, 2022, **7**, 16547–16560.

21 A. Fuior, D. Cebotari, O. Garbuz, S. Calancea, A. Gulea and S. Floquet, *Inorg. Chim. Acta*, 2023, **548**, 121372.

22 D. Cebotari, J. Buils, O. Garbuz, G. Balan, J. Marrot, V. Guérineau, D. Touboul, M. Haouas, M. Segado-Centelles, C. Bo, A. Gulea and S. Floquet, *J. Inorg. Biochem.*, 2023, **245**, 112258.

23 D. Cebotari, S. Calancea, J. Marrot, R. Guillot, C. Falaise, V. Guérineau, D. Touboul, M. Haouas, A. Gulea and S. Floquet, *Dalton Trans.*, 2023, **52**, 3059–3071.

24 T. Straistari, R. Hardré, J. Fize, S. Shova, M. Giorgi, M. Réglier, V. Artero and M. Orio, *Chem. – Eur. J.*, 2018, **24**, 8779–8786.

25 J. Mehrez, A. Barrozo, L. Delmotte, R. Hardre, M. Papadakis and M. Orio, *Dalton Trans.*, 2025, **54**, 8113–8122.

26 M. Papadakis, G. Landrou, M. Poisson, L. Delmotte, K. Achileos, S. Bertaina, R. Hardre, K. Ladomenou, A. Coutsolelos and M. Orio, *Eur. J. Inorg. Chem.*, 2023, **26**, e202300352.

27 T. Straistari, J. Fize, S. Shova, M. Réglier, V. Artero and M. Orio, *ChemCatChem*, 2017, **9**, 2262–2268.

28 M. Papadakis, A. Barrozo, L. Delmotte, T. Straistari, S. Shova, M. Réglier, V. Krewald, S. Bertaina, R. Hardré and M. Orio, *Inorganics*, 2023, **11**, 149.

29 M. Papadakis, J. Mehrez, I. Wehrung, L. Delmotte, M. Giorgi, R. Hardré and M. Orio, *ChemCatChem*, 2024, **16**, e202400426.

30 S. Cronin, A. Al Mamun, M. Toda, M. Mashuta, Y. Losovyj, P. Kozlowski, R. Buchanan and C. Grapperhaus, *Inorg. Chem.*, 2019, **58**, 12986–12997.

31 G. M. Sheldrick, *SADABS program for scaling and correction of area detector data*, 1997.

32 G. M. Sheldrick, *Acta Crystallogr., Sect. C: Struct. Chem.*, 2015, **71**, 3–8.

33 C. B. Hübschle, G. M. Sheldrick and B. Dittrich, *J. Appl. Crystallogr.*, 2011, **44**, 1281–1284.

34 E. Van Lenthe and E. Baerends, *J. Comput. Chem.*, 2003, **24**, 1142–1156.

35 J. Perdew, *Phys. Rev. B:Condens. Matter Mater. Phys.*, 1986, **33**, 8822–8824.

36 A. Becke, *Phys. Rev. A*, 1988, **38**, 3098–3100.

37 S. Grimme, J. Antony, S. Ehrlich and H. Krieg, *J. Chem. Phys.*, 2010, **132**, 154104.

38 E. Vanlenthe, E. Baerends and J. Snijders, *J. Chem. Phys.*, 1993, **99**, 4597–4610.

39 C. Pye and T. Ziegler, *Theor. Chem. Acc.*, 1999, **101**, 396–408.

40 A. Klamt, *J. Phys. Chem.*, 1995, **99**, 2224–2235.

41 M. Álvarez-Moreno, C. de Graaf, N. López, F. Maseras, J. M. Poblet and C. Bo, *J. Chem. Inf. Model.*, 2015, **55**, 95–103.

42 H. R. Darabi, S. Rastgar, K. Aghapoor and F. Mohsenzadeh, *Monatsh. Chem.*, 2018, **149**, 1121–1124.

43 J. C. Kemmegne-Mbouguen, S. Floquet and E. Cadot, *C. R. Chim.*, 2021, **24**, 91–101.

44 Z. Han, Y. Gao, J. Wang and C. Hu, *Z. Anorg. Allg. Chem.*, 2009, **635**, 2665–2670.

45 R. Thangamuthu, Y. Wu and S. Chen, *Electroanalysis*, 2009, **21**, 1655–1658.

46 V. R. Ott, D. S. Swieter and F. A. Schultz, *Inorg. Chem.*, 1977, **16**, 2538–2545.

47 F. A. Schultz, V. R. Ott, D. S. Rolison, D. C. Bravard, J. W. McDonald and W. E. Newton, *Inorg. Chem.*, 1978, **17**, 1758–1765.

48 A. Kuhn, K. von Eschwege and J. Conradie, *J. Phys. Org. Chem.*, 2012, **25**, 58–68.

49 R. Nicholson, *Anal. Chem.*, 1966, **38**, 1406.

50 T. F. Beltran, M. Feliz, R. Llusar, J. A. Mata and V. S. Safont, *Organometallics*, 2011, **30**, 290–297.

51 A. G. Algarra, M. G. Basallote, M. J. Fernandez-Trujillo, M. Feliz, E. Guillamon, R. Llusar, I. Sorribes and C. Vicent, *Inorg. Chem.*, 2010, **49**, 5935–5942.

52 A. Appel, D. DuBois and M. DuBois, *J. Am. Chem. Soc.*, 2005, **127**, 12717–12726.

53 N. Queyriaux, N. Durvin, D. Leon, M. Boegli, L. Vendier and A. Simonneau, *Eur. J. Inorg. Chem.*, 2023, e202300426.

54 M. Xue, Z. Peng, K. Tao, J. Jia, D. Song, C. Tung and W. Wang, *Nat. Commun.*, 2024, **15**, 797.

55 N. Lakshan, D. Aluthge and W. Sameera, *Catalysts*, 2024, **14**, 816.